PLOS COMPUTATIONAL BIOLOGY

RESEARCH ARTICLE

Quantification of long-term doxorubicin response dynamics in breast cancer cell lines to direct treatment schedules

Grant R. Howard[1], **Tyler A. Jost**[1], **Thomas E. Yankeelov**[1,2,3,4,5,6], **Amy Brock**[1,7]*

1 Department of Biomedical Engineering, The University of Texas at Austin, Austin, Texas, United States of America, **2** Department of Diagnostic Medicine, The University of Texas at Austin, Austin, Texas, United States of America, **3** Department of Oncology, The University of Texas at Austin, Austin, Texas, United States of America, **4** Oden Institute for Computational Engineering and Sciences, The University of Texas at Austin, Austin, Texas, United States of America, **5** Livestrong Cancer Institutes, The University of Texas at Austin, Austin, Texas, United States of America, **6** Department of Imaging Physics, The University of Texas MD Anderson Cancer Center, Houston, Texas, United States of America, **7** Department of Cell and Molecular Biology, The University of Texas at Austin, Austin, Texas, United States of America

* amy.brock@utexas.edu

Citation: Howard GR, Jost TA, Yankeelov TE, Brock A (2022) Quantification of long-term doxorubicin response dynamics in breast cancer cell lines to direct treatment schedules. PLoS Comput Biol 18(3): e1009104. https://doi.org/10.1371/journal.pcbi.1009104

Editor: Stacey Finley, University of Southern California, UNITED STATES

Received: May 16, 2021

Accepted: February 7, 2022

Published: March 31, 2022

Data Availability Statement: All raw and processed data in this manuscript, as well as all computational code used for model calibration and validation, are publicly available at https://github.com/brocklab/Drug-Response-Dynamics-Model-Calibration.

Funding: We are grateful for funding through the NIH via R01CA226258 and U01CA253540 to A.B. and NIH U01CA142565, U01CA174706, U24CA226110, R01CA240589, and CPRIT RR160005 to T.E.Y. T.E.Y. is a CPRIT Scholar of

Abstract

While acquired chemoresistance is recognized as a key challenge to treating many types of cancer, the dynamics with which drug sensitivity changes after exposure are poorly characterized. Most chemotherapeutic regimens call for repeated dosing at regular intervals, and if drug sensitivity changes on a similar time scale then the treatment interval could be optimized to improve treatment performance. Theoretical work suggests that such optimal schedules exist, but experimental confirmation has been obstructed by the difficulty of deconvolving the simultaneous processes of death, adaptation, and regrowth taking place in cancer cell populations. Here we present a method of optimizing drug schedules in vitro through iterative application of experimentally calibrated models, and demonstrate its ability to characterize dynamic changes in sensitivity to the chemotherapeutic doxorubicin in three breast cancer cell lines subjected to treatment schedules varying in concentration, interval between pulse treatments, and number of sequential pulse treatments. Cell populations are monitored longitudinally through automated imaging for 600–800 hours, and this data is used to calibrate a family of cancer growth models, each consisting of a system of ordinary differential equations, derived from the bi-exponential model which characterizes resistant and sensitive subpopulations. We identify a model incorporating both a period of growth arrest in surviving cells and a delay in the death of chemosensitive cells which outperforms the original bi-exponential growth model in Akaike Information Criterion based model selection, and use the calibrated model to quantify the performance of each drug schedule. We find that the inter-treatment interval is a key variable in determining the performance of sequential dosing schedules and identify an optimal retreatment time for each cell line which extends regrowth time by 40%-239%, demonstrating that the time scale of changes in chemosensitivity following doxorubicin exposure allows optimization of drug scheduling by varying this inter-treatment interval.

Cancer Research. The funders had no role in study design, data collection and analysis, decision to publish, or preparation of the manuscript.

Competing interests: The authors have declared that no competing interests exist.

Author summary

Acquired chemoresistance is a common cause of treatment failure in cancer. The scheduling of a multi-dose course of chemotherapeutic treatment may influence the dynamics of acquired chemoresistance, and drug schedule optimization may increase the duration of effectiveness of a particular chemotherapeutic agent for a particular patient. Here we present a method for experimentally optimizing an *in vitro* drug schedule through iterative rounds of experimentation and computational analysis, and demonstrate the method's ability to improve the performance of doxorubicin treatment in three breast carcinoma cell lines. Specifically, we find that the interval between drug exposures can be optimized while holding drug concentration and number of treatments constant, suggesting that this may be a key variable to explore in future drug schedule optimization efforts. We further use this method's model calibration and selection process to extract information about the underlying biology of the doxorubicin response, and find that the incorporation of delays on both cell death and regrowth are necessary for accurate parameterization of cell growth data.

Introduction

Cancer is the second most prevalent cause of death in the United States, and acquired chemoresistance is a common cause of treatment failure in cancer [1,2]. While many studies have investigated the biochemical mechanisms of chemoresistance, predicting the onset of resistance and the population dynamics of sensitive and resistant cells remains a challenge [3–6].

Early chemotherapy treatment schedules, based on the approach of maximally-tolerated dose to achieve maximal killing of tumor cells, assumed a homogenous, exponentially growing cell population [7,8]. Subsequent studies have pointed to the significance of intratumor heterogeneity in cell growth rate and drug sensitivity [9–18]. Norton and others established that tumor kill is proportional to growth rat [19–21], and adjuvant chemotherapy schedules for breast cancer were revised to decrease the interval of therapy for fast-growing TNBC [22–24]. Other studies point to metronomic therapy and adaptive therapy as potential improvements for breast cancer scheduling [25–29].

Mathematical modeling of drug responses has developed optimal solutions for drug dosing under a variety of model assumptions [30–34], highlighting the opportunity to improve cancer treatment by optimizing drug schedules. However, these efforts have generally been purely theoretical. Under the necessarily simplified assumptions of these drug sensitivity models, it is possible to find a true mathematical optimum, but these studies have not explored the magnitude or form of deviation between their models and experimental observations. This reveals a need for methods to experimentally test the response to drug schedules, and to use those experimental results to inform and calibrate models of drug response in cancer. Robust predictive models of drug response are a necessary step towards the ultimate goal of patient-specific predictive models of therapy-response and relapse.

A challenge in modeling chemoresistance is that the state of drug sensitivity is often represented as binary–sensitive or resistant. Clinically, resistance is usually inferred at very coarse time intervals–a patient is retrospectively assessed as sensitive or resistant to a course of treatment as a whole. In *in vitro* work, cell lines are labeled as sensitive or resistant as well, based on their stable drug sensitivity [35,36]. This approach may obscure key underlying characteristics of the system if drug sensitivity is heterogeneous in the cancer cell population. In addition, cells may change drug sensitivity over time or in response to environmental conditions, adding temporal heterogeneity [37–42]. The consequence is that cells display a distribution of responses to drug exposure and this distribution may vary with time [43–51]. Experimental work describing the distribution of drug sensitivity in cancer cell populations, and the temporal changes arising from cell plasticity, is key to understanding drug resistance at the population level.

In this work, we seek to quantify the dynamic changes in drug sensitivity following treatment to iteratively optimize treatment schedules in a series of *in vitro* experiments subjecting three breast cancer cell lines to a series of pulsed drug perturbations which vary in drug concentration, inter-treatment interval, and number of serial drug exposures. Long-term automated time-lapse microscopy enables quantitation of population dynamics in multiple replicates, doses and regimens over days to weeks. Here we measured up to 12 individual culture wells in 3 cell types treated with a range of 9 doses and 13 regimens.

By calibrating the resulting data to a mathematical model, we quantify the distribution of the underlying populations with respect to model parameters of interest including resistant fraction, relapse growth rate, and sensitive cell death rate. Additionally, we characterize the dynamics of both the relapse and dying populations. In this study, we sought to capture the fact that sensitive cells do not respond to drug treatment by immediately undergoing cell death and resistant cells do not respond by continuing to proliferate at the same rate as untreated cells. Rather, the processes of cell death, cell cycle arrest, and cell growth after treatment are complex and these time scales may overlap—with some cells continuing to die in response to drug treatment, while others are simultaneously recovering from a period of arrest and beginning to proliferate.

Model selection is used to identify three phenomenological models which vary in the dynamics defining cell growth and death in treated populations, and which can be used to parameterize the data. Time-lapse microscopy data is used to calibrate the three phenomenological models, and select the model which best characterizes the data. The optimal model is then used to quantify the impact of the tested drug schedules on cancer cell population, and identify schedules with superior performance. This demonstrates a method for optimizing drug schedules using mathematical models of drug sensitivity which are experimentally calibrated using high throughput in-vitro experiments. This method could be extended to additional drugs, drug combinations, and cancer types.

Results

Model description

We used a mathematical model, described by a system of ordinary differential equations, which treats cancer cell population dynamics as a process consisting of a decreasing drug-sensitive subpopulation of tumor cells, and an independently growing drug-resistant subpopulation. This model has successfully described tumor dynamics in non-small cell lung cancer, melanoma [52], multiple myeloma [53], and ovarian cancer [54]. After exposure to drug, the net fitness of the drug-sensitive (S) cells is represented in terms of an exponential decay or "tumor cell kill" rate k, and the net fitness of the resistant (R) cancer cells as an exponential growth rate $g_r > 0$, and the initial fraction of drug-resistant cells by $0 \leq f_r \leq 1$. Additionally, the resistant cancer cells may experience a period of proliferation arrest $t_r \geq 0$ (**Fig 1A**). The R and S designations are solely with respect to the specific drug exposure being examined, and are not intended to specify any particular mechanism of action. To analyze the response of a population of S and R cells to drug treatment, we use a system of two ordinary differential Eqs (1 and 2) coupled by the total cell number (Eq 3) to describe the dynamics of the S and R

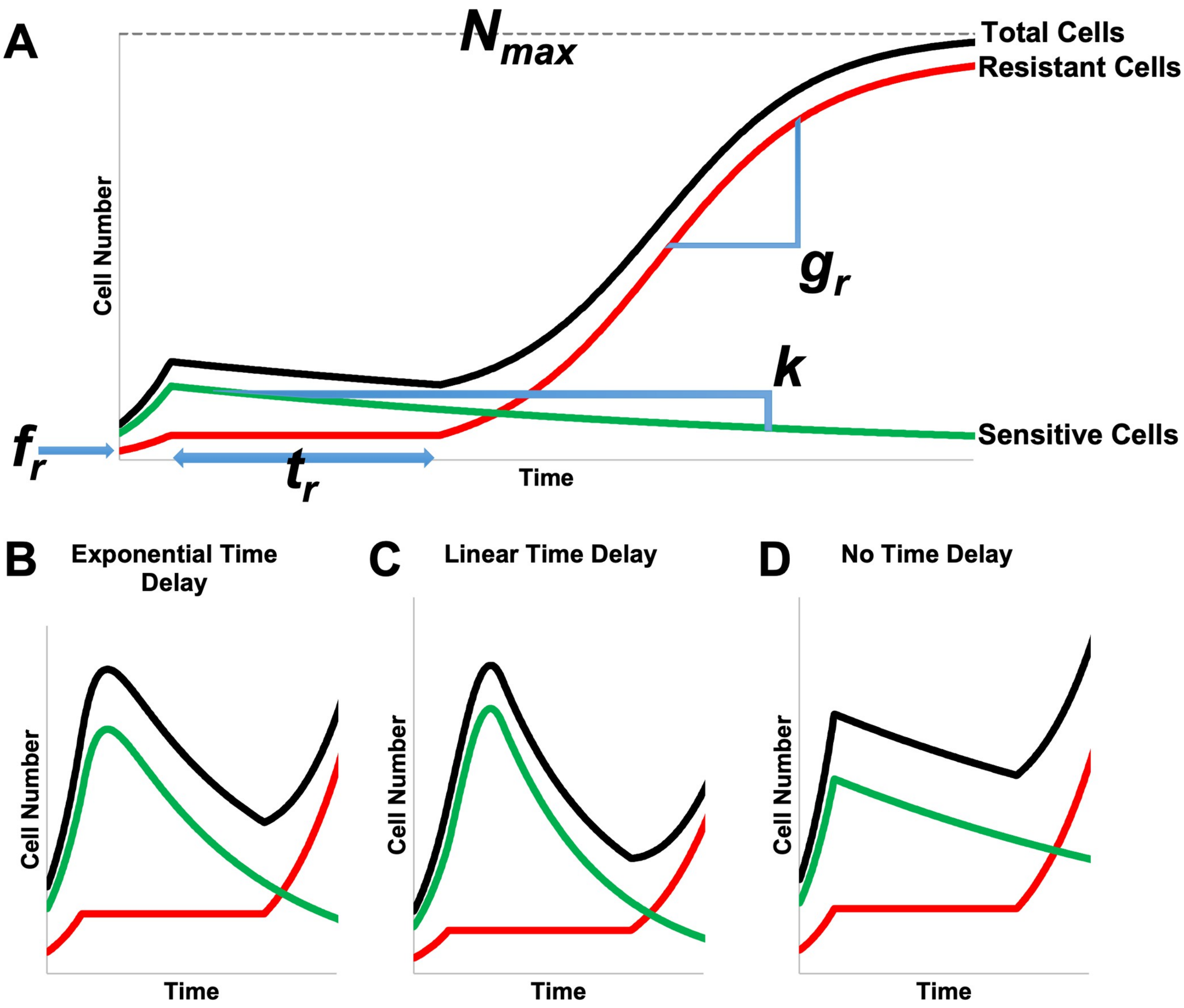

Fig 1. Schematic illustration of model structures with curves for total cell number (black) partitioned into resistant (red) and sensitive (green) fractions. Regions of the curves are marked to show the effects of key model parameters (A). The effects of three different models of *k* are shown for model 1 with an exponential time delay on *k* (B), model 2 with a linear time delay on *k* (C) or model 3 with no time delay on *k* (D).

https://doi.org/10.1371/journal.pcbi.1009104.g001

subpopulations.

$$\frac{dR}{dt} = g_r R\left(1 - \frac{N}{N_{max}}\right)H(t - t_r) \tag{1}$$

$$\frac{dS}{dt} = -k(t)S \tag{2}$$

$$N = R + S \tag{3}$$

Initial conditions are specified using the resistant fraction, f_r, in Eqs 4 and 5. $H(x)$ is the Heaviside step function, which is 0 for negative values of the argument and 1 for positive values of the argument.

$$R(t_0) = f_r N_0 \tag{4}$$

$$S(t_0) = (1 - f_r) N_0 \tag{5}$$

To better understand how growth and death dynamics impact drug sensitivity of the overall cell population, we use automated image analysis of time lapse microscopy data to calibrate parameters (**Table 1**) for three families of phenomenological models of the population-level drug response. Resistant cells experience a period of growth arrest, t_r, followed by logistic growth at rate, g_r. Sensitive cells die at rate k, which is subject to variation in the doxorubicin response [55], and three models for k are considered: 1) a time-delayed model of k, such that the value varies between cell growth at the initial growth rate of g_0 and cell death at a maximum rate of k_d with exponential decay from g_0 to k_d at a time constant of t_d (Eq 6) (**Fig 1B**), 2) a time-delayed model of k such that the value varies linearly between cell growth at the initial growth rate of g_0 and cell death at a maximum rate of k_d over a total time of t_d (Eq 7) (**Fig 1C**), 3) a constant value of k (Eq 8, **Fig 1D**). Models 1 and 2 each include 6 total parameters, while the simpler model 3 includes 4.

$$k = k_d - (g_0 + k_d) exp\left(-\frac{t}{t_d}\right) \tag{6}$$

$$k = k_d - (g_0 + k_d)\left(1 - \frac{t}{t_d}\right) H(t_d - t) \tag{7}$$

$$k = k_d \tag{8}$$

Model 1 represents a case in which cells transition from proliferating to dying probabilistically after treatment. At the time of treatment, the cell population is still proliferating (represented in the model as a negative net death rate for this cell compartment). The probabilistic behavior of individual cells, when evaluated over the cell population, results in a smooth transition in the net death rate from proliferation to death and approaches the maximum value of k_d exponentially at a time constant of t_d. Model 2 represents a case where cells take time, t_d, to halt proliferation, again transitioning from initially proliferating at a rate of g_0 at the time drug exposure begins, to an eventual maximum death rate of k_d. Model 3 represents the simplest

Table 1. Summary of model parameters. Parameters were either calibrated from growth data (see Methods - Model Calibration) or determined from longitudinal cell growth data (see Methods - Quantification of t_r).

Symbol	Model Parameter Description	Parameter Assignment
f_r	Resistant fraction	Calibrated
g_r	Post-treatment growth rate	Calibrated
t_r	Proliferation delay	Measured via clustering analysis
k_d	Sensitive cell death rate	Calibrated
t_d	Time constant for death delay	Calibrated
g_0	Pre-treatment growth rate	Calibrated
N_{max}	Carrying capacity	Calibrated

https://doi.org/10.1371/journal.pcbi.1009104.t001 case with the minimum number of parameters; here the population responds to drug exposure rapidly enough on the time scale of the experiment for transition time to be negligible. These are nested models, and we will evaluate the need for the additional parameters, which increase the complexity of the models, using model selection criteria when fitting the data to the models.

Model identifiability

To test the ability of our modeling framework to accurately extract parameter values and select among models, each model within the family described above was used to calibrate simulated data. This model family includes three sets of assumptions concerning the form of the sensitive cell death rate k, which are described as models 1, 2, and 3. Independently, the proliferation delay t_r can be zero or non-zero, and if non-zero, t_r can be calibrated or given as input. Finally, the carrying capacity N_{max} can be calibrated or fixed. Model identifiability techniques were used to investigate the ability of each of the 18 models that these assumptions generate to extract information from simulated data sets (see **Text A in S1 File**). A set of three models varying only in the handling of the sensitive cell death rate were identified, which demonstrated the greatest ability to extract parameter values from simulated data sets with known ground truth (**Table 2**).

A key finding from this model identifiability work was that if a proliferation delay is present in the ground truth model ($t_r \neq 0$), the proliferation delay must be given as model input to extract accurate parameter values. The question of whether t_r is in fact non-zero must be resolved experimentally, as computational work alone proved unable to determine this in the analysis stage. Examination of the raw data demonstrated that the period of proliferation arrest, t_r, can be non-zero, and in some cases is substantial (**Fig 2**).

The Akaike information criterion [56,57] (AIC) was applied to the calibrations generated in this model identifiability analysis to test its ability to identify the underlying model structure in cases where the ground truth is known independently. When the AIC is computed for three otherwise equivalent models which vary in the form of k, it selects the model which matches the ground truth of the simulated data in 97% of cases where there is no death delay, in 87% of cases if the death delay has an exponential form, and in 84% of cases when the death delay has a linear form. In each case, the correct model is identified in a majority of simulated data sets, demonstrating the utility of the AIC at identifying the model which best matches the ground truth.

Quantification of long term population level response

To determine the dynamics of the long-term cell population response to doxorubicin, breast cancer cell populations were subjected to one to five sequential doxorubicin exposures, with the drug concentration, interval between drug exposures, or number of drug exposures allowed to vary. Time lapse microscopy and automated image analysis was used to quantify the cell number throughout the treatment period and up to four weeks after the final dose.

Table 2. Summary of model assumptions in models selected for further analysis.

Model	Assignment of t_r, proliferation delay in R cells	k, death delay in S cells	N_{max}
1	known and given as input	Exponential	Calibrated
2	known and given as input	Linear	Calibrated
3	known and given as input	None	Calibrated

https://doi.org/10.1371/journal.pcbi.1009104.t002

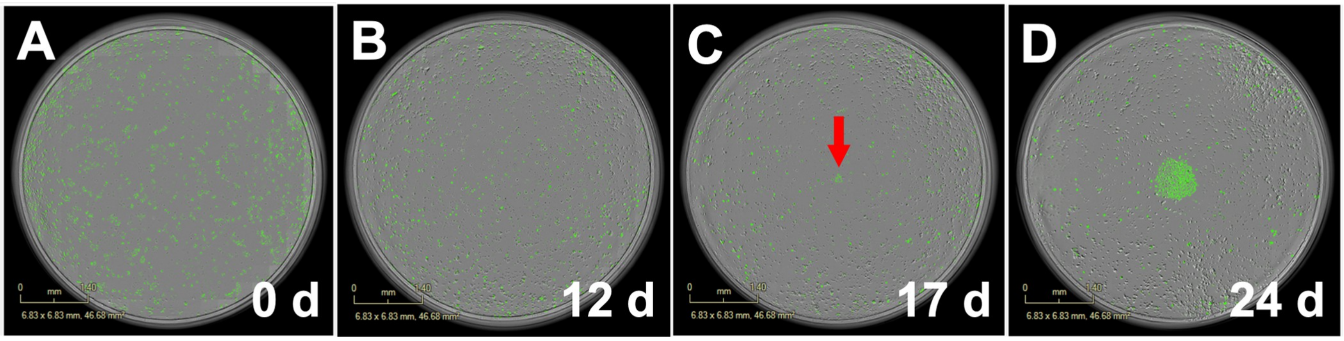

Fig 2. Micrograph example illustrating doxorubicin induced proliferation delay. In this example demonstrating a doxorubicin induced proliferation delay, after exposure to 150 nM doxorubicin at time 0 (A) MCF7 cells stop proliferating and remain in arrest for 315 hours. At 14 days (B), cells have died off in the intervening time, and proliferation has not occurred, and at 21 days (C), proliferation has produced a small patch of cells indicated by the red arrow; proliferation then continues and produces a patch of hundreds of cells by 28 days (D). Untreated cells grow to confluence in approximately four days.

https://doi.org/10.1371/journal.pcbi.1009104.g002

The long term response to a 24 hour doxorubicin pulse varies not only with drug concentration (Fig 3A, 3D**, and** 3G), but also with the cell population's history of previous exposure, even if the total dose delivered remains constant (Fig 3B, 3C, 3E, 3F, 3H, and 3I). Population behavior varies over time, and the response observed at any single time point (such as 48 or 72 hours, which are frequently chosen as endpoints for single time-point observations) does not accurately characterize the overall dynamic response. Visual assessment of these cell number curves offers some intuition on the relative strength of the drug treatments: A cell population that is sensitive to a drug treatment may manifest in a curve that dips to a deeper minimum, or takes longer to resume net population growth, or shows slower population growth over the long term. As expected, for a single administration of doxorubicin, these effects of treatment increase with dose (Fig 3A, 3D, and 3G). When multiple doses of the same concentration are administered, the total amount of drug increases with the number of exposures; this generates the similarly intuitive result that the impact of the treatment increases when going from one treatment to two sequential treatments (Fig 3C, 3F, and 3I).

When the total drug exposure for each treatment group is held constant while the interval between the two exposures is varied, the cell population response curves vary considerably (Fig 3B, 3E, and 3H). This indicates that the drug sensitivity of all three cell lines varies dynamically, such that the timing of a second drug exposure has a profound effect on the effectiveness of the second treatment. While these observations can be made on a qualitative level from the cell number curves, calibrating these experimental results to the models discussed above allows for quantitative investigation of the variation in response.

Fraction of non-recovering replicates

Under some treatment regimens, we observe a bifurcation in the response: some replicate cultures recover proliferative capacity during the experiment, while others do not (and therefore exhibit only cell death throughout the experiment). This necessitates split handling of the analysis as well, since the resistant population properties cannot be obtained in cases where no cells were resistant to the treatment. The percentage of replicate cultures which do not recover in each treatment group is shown in Fig 4, and these wells are excluded from the analysis of resistant cell populations. This is accomplished by fixing f_r and g_r at 0 when fitting non-recovering replicates, and by performing further analysis of resistant populations using only the fitted parameters from recovering replicates. This allows us to extract information about the sensitive population from non-recovering replicates without contaminating analysis of the resistant population.

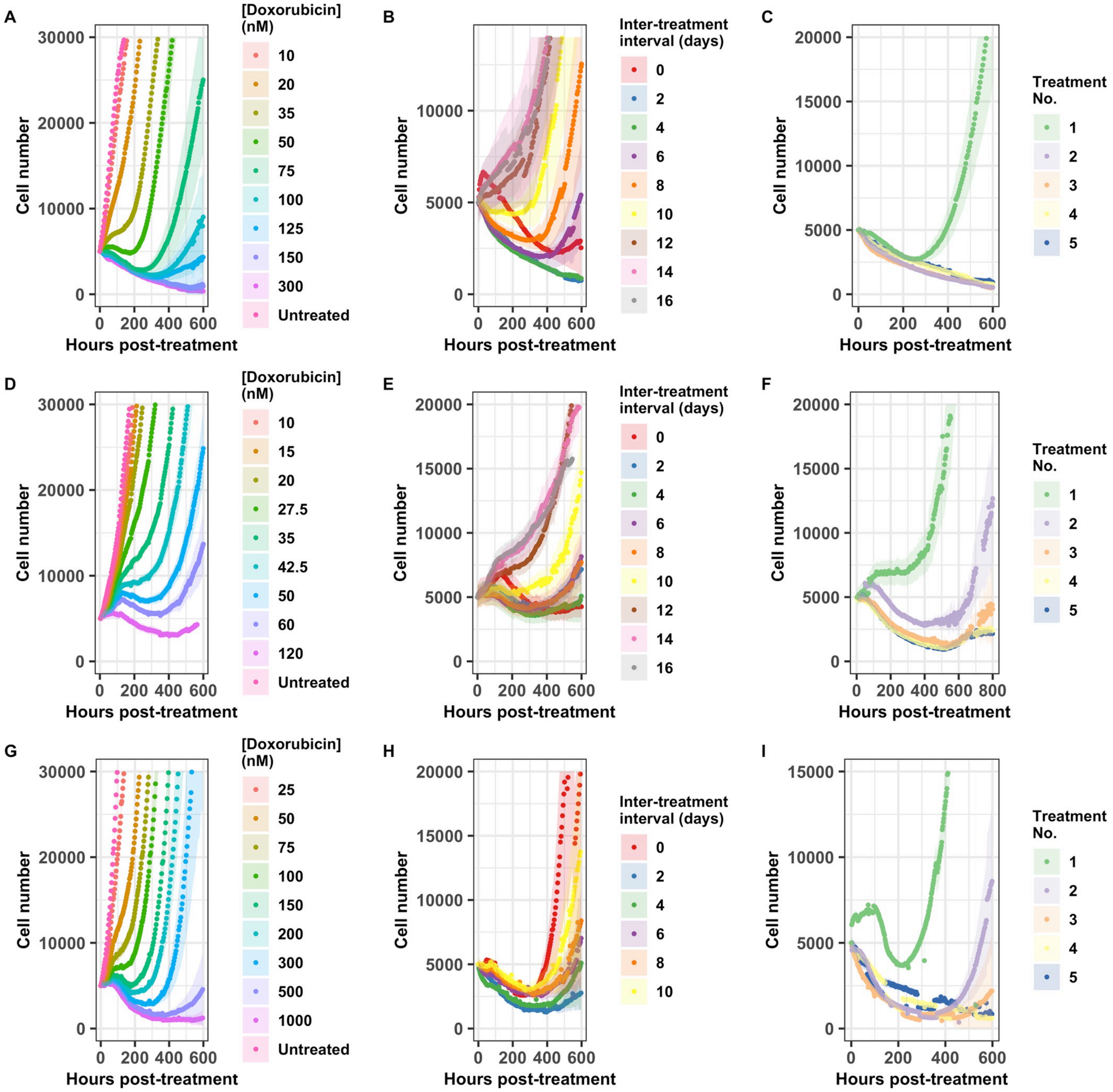

Fig 3. Cell population response to doxorubicin regimens. Population level response to 24 hour doxorubicin exposures is quantified as doxorubicin concentration varies in the MCF7 cell line (A), the BT474 cell line (D), and the MDA-MB-231 cell line (G), as the interval between two 24 hour doxorubicin exposures varies at 75 nM in the MCF7 cell line (B), at 35 nM in the BT474 cell line (E), and at 200 nM in the MDA-MB-231 cell line (H), and as the number of sequential 24 hour doxorubicin exposures varies at a two day interval and 75 nM in the MCF7 cell line (C), at a zero day interval (continuous exposure) and 35 nM in the BT474 cell line (F), and at a two day interval and 200 nM in the MDA-MB-231 cell line (I). Each curve represents the average of six (A, D, G) or 12 (B, C, E, F, H, I) replicate samples, and 95% confidence intervals are marked by the shaded regions. All curves are aligned such that $t = 0$ is the beginning of the final drug exposure for that treatment group.

https://doi.org/10.1371/journal.pcbi.1009104.g003

Although this phenomenon hinders analysis of some resistant cell properties, it also reveals which treatment regimens are capable of eliminating the entire experimental cancer cell population. The bifurcation indicates that these treatments should not be assumed to be completely

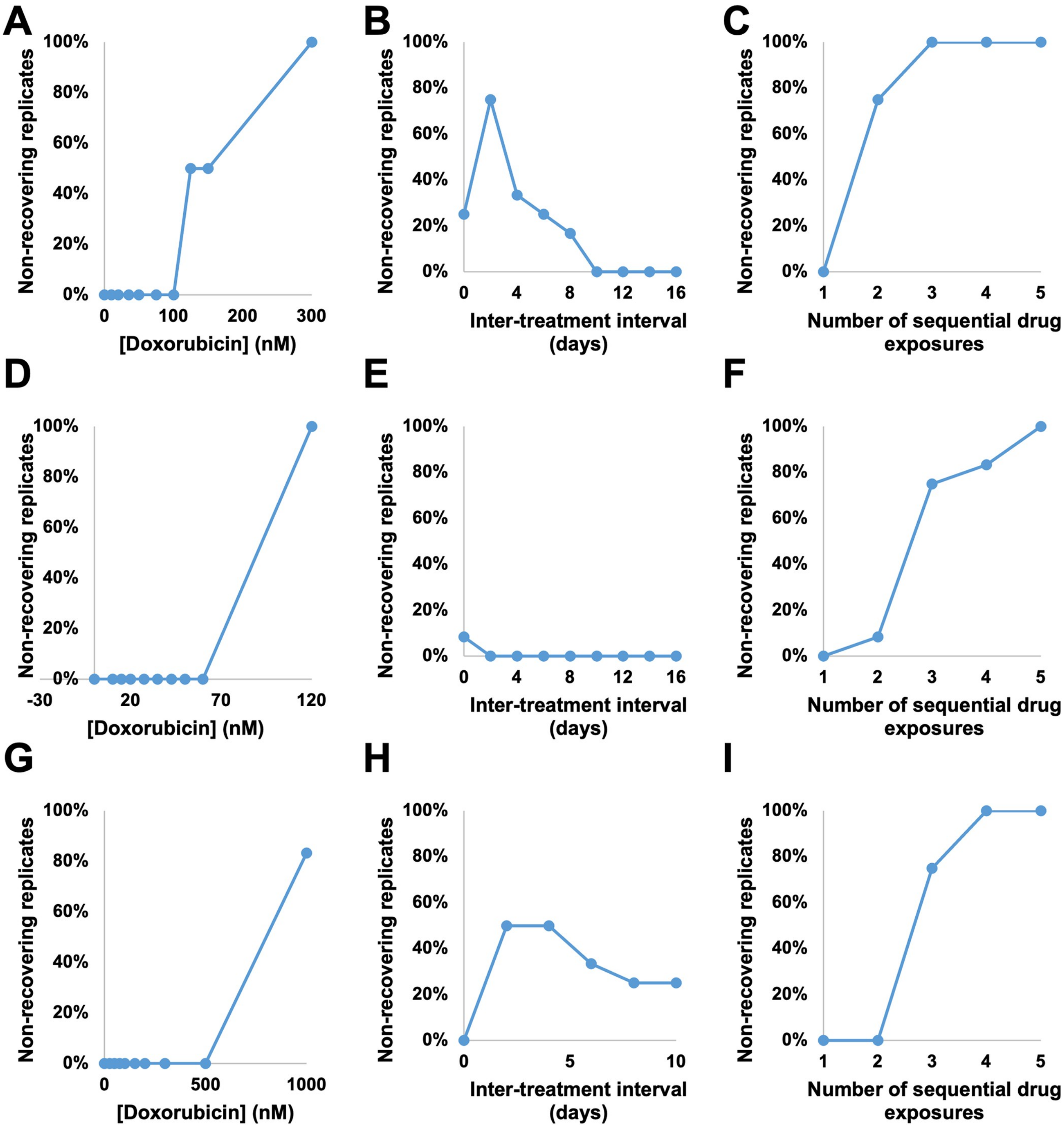

Fig 4. Percentage of non-recovering replicate cell populations. The percentage of replicate cultures which did not recover during the course of the experiment is shown as doxorubicin concentration varies in the MCF7 cell line (A), the BT474 cell line (D), and the MDA-MB-231 cell line (G), as the interval between two 24 hour doxorubicin exposures varies at 75 nM in the MCF7 cell line (B), at 35 nM in the BT474 cell line (E), and at 200 nM in the MDA-MB-231 cell line (H), and as the number of sequential 24 hour doxorubicin exposures varies at a two day interval and 75 nM in the MCF7 cell line (C), at a zero day interval (continuous exposure) and 35 nM in the BT474 cell line (F), and at a two day interval and 200 nM in the MDA-MB-231 cell line (I). Each value is the percentage of 6 (A, D, G) or 12 (B, C, E, F, H, I) replicates.

https://doi.org/10.1371/journal.pcbi.1009104.g004

effective against the cancer cell population; rather, it is sufficient for cells that are resistant to the treatment in question to be rare enough in the population as a whole that the initial population of approximately 2,000 seeded cells is too low to ensure that such a resistant cell will be present. Despite this caveat, these conditions do represent the practical limits of treatment regimens that can be investigated in the 96 well format. In the MCF7 cell line, doxorubicin concentrations of 125 nM or higher may result in non-recovering replicates (**Fig 4A**), and two or more sequential treatments at 75 nM may result in non-recovering replicates (**Fig 4C**). In the BT474 cell line, a doxorubicin concentration of 120 nM resulted in no recovering wells (**Fig 4D**), and two or more sequential exposures to 35 nM doxorubicin resulted in some non-recovering wells (**Fig 4F**). Similarly, in the MDA-MB-231 cell line, doxorubicin at a concentration of 1 μM (**Fig 4G**) or three or more exposures to 200 nM doxorubicin (**Fig 4I**) may result in non-recovering replicates. While the concentration thresholds vary from cell line to cell line, in each of these cases the fraction of non-recovering wells increases with the total drug exposure within a cell line.

When the inter-treatment interval is varied with the total drug exposure held constant, we find that the fraction of non-recovering wells peaks in the MCF7 cell line at 75% (nine replicates out of 12) with a two day interval (**Fig 4B**), then declines to 0% at intervals of 10 or more days. In the BT474 cell line, 8% (one replicate out of 12) fails to recover in the zero interval (continuous treatment) group, with all wells recovering at longer intervals (**Fig 4E**). In the MDA-MB-231 cell line, the fraction of wells which do not recover peaks at 50% (six out of 12 replicate wells) at an interval of 2 or 4 days, and declines at longer intervals (**Fig 4H**). In each cell line this again suggests that the drug sensitivity of these populations varies dynamically over this period of approximately two weeks after an initial drug exposure.

Proliferation delay, t_r

The model identifiability analysis demonstrates that, if a period of growth arrest is present in experimental data, then it must be incorporated into the growth model to obtain accurate parameter values *via* model calibration (**Text A Figure C in S1 File**). Growth arrest does occur under some of the treatment regimens investigated in this series of experiments. Density based clustering analysis using DBSCAN [58] with manual correction for common errors is used to identify the restart of proliferation in replicate cultures which experience a period of growth arrest (**Fig 5**). When the concentration of doxorubicin in a single exposure is varied, a threshold is observed with concentrations of 50 nM or higher inducing growth arrest in the MCF7 cell line (**Fig 5A**), concentrations of 42.5 nM of higher inducing growth arrest in the BT474 cell line (**Fig 5D**), and concentrations of 150 nM or higher inducing growth arrest in the MDA-MB-231 cell line (**Fig 5G**). In the MCF7 cell line, when the interval between two 75 nM doxorubicin exposures is varied, the period of growth arrest decreases as the inter-treatment interval increases (**Fig 5B**), with intervals of 0–4 days experiencing over 200 hours of growth arrest and with some replicates at intervals of 8 or more days experiencing no growth arrest at all; since an initial 75 nM exposure results in approximately 125 hours of growth arrest, this suggests dynamic variation in drug sensitivity over this period of approximately two weeks. Likewise, in the BT474 cell line, as the interval between two 35 nM doxorubicin exposures is varied the period of growth arrest decreases with intervals of 10 days or longer resulting in no growth arrest (**Fig 5E**). Similarly, when the MDA-MB-231 cell line is exposed to two 200 nM drug pulses, the period of growth arrest is elevated for at least 10 days, with a peak of over 400 hours with a two day interval between exposures (**Fig 5H**). When the number of sequential drug exposures at a two day interval is varied, the period of growth arrest increases significantly after a second treatment in the MCF7 cell line (**Fig 5C**), the BT474 cell line (**Fig 5F**), and the MDA-MB-231 cell line (**Fig 5I**).

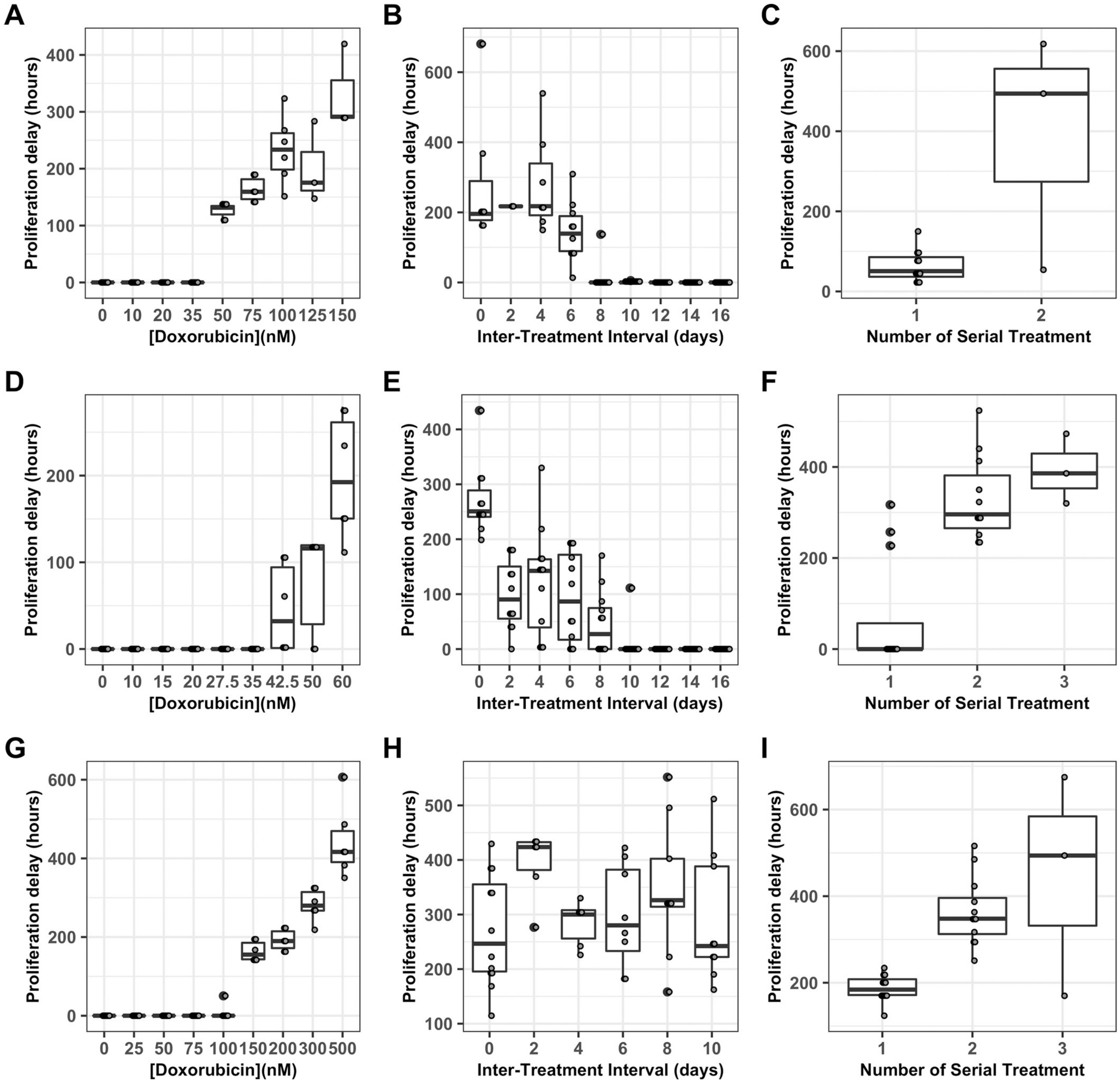

Fig 5. Proliferation delay, t_r varies with dosing regimen. Length of growth arrest of resistant cells (t_r) is displayed as a Tukey box-and-whiskers plot as doxorubicin concentration varies in the MCF7 cell line (A), the BT474 cell line (D), and the MDA-MB-231 cell line (G), as the interval between two 24 hour doxorubicin exposures varies at 75 nM in the MCF7 cell line (B), at 35 nM in the BT474 cell line (E), and at 200 nM in the MDA-MB-231 cell line (H), and as the number of sequential 24 hour doxorubicin exposures varies at a two day interval and 75 nM in the MCF7 cell line (C), at a zero day interval (continuous exposure) and 35 nM in the BT474 cell line (F), and at a two day interval and 200 nM in the MDA-MB-231 cell line (I). The number of replicates in each group varies between 3 and 12; all replicates in which recovery is observed are included (see Fig 4).

https://doi.org/10.1371/journal.pcbi.1009104.g005

Model selection

AIC values are calculated for each replicate culture for models 1 (exponential death delay), 2 (linear death delay), and 3 (no death delay); the AIC allows comparison of the goodness of fit for models with varying numbers of free parameters. Across 648 replicate cultures calibrated

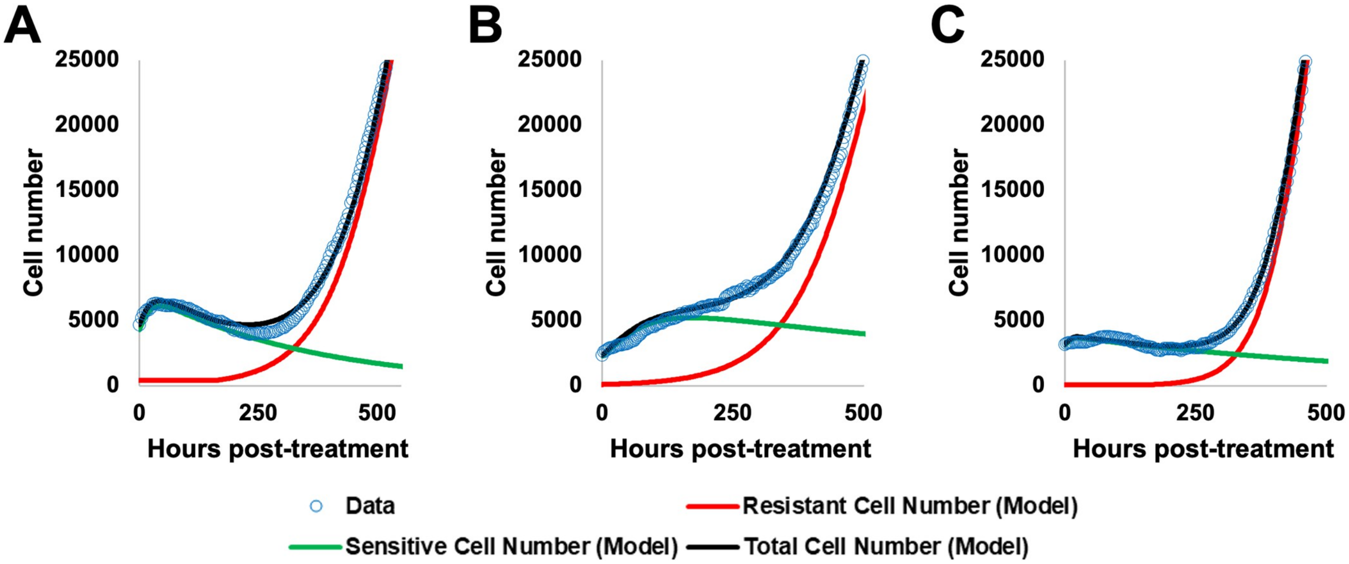

Fig 6. Examples of model fitting demonstrate the ability of model 1 to capture long term dynamics. Examples of model fitting are shown for a single replicate culture in the MCF7 (A), BT474 (B), and MDA-MB-231 (C) cell lines. The curve represents a response to the doxorubicin concentration used in serial treatment within the cell line– 75 nM for the MCF7 line, 35 nM for the BT474 cell line, and 200 nM for the MDA-MB-231 cell line. Data is shown as open blue circles, while the best-fit curve for model 1 (the total number of sensitive and resistant cells) is shown in black, with the resistant and sensitive compartments shown in red and green respectively.

https://doi.org/10.1371/journal.pcbi.1009104.g006

to models 1, 2, and 3, the AIC indicates that model 1 is optimal in 382 replicates (59.0%), model 2 is optimal in 129 replicates (19.9%), and model 3 is optimal in 137 replicates (21.1%). This suggests that model 1 achieves the best overall performance across the range of conditions analyzed; however, models 2 and 3 are selected in a substantial minority of cases.

Although model 1 is able to capture cell growth dynamics in all three cell lines (Fig 6), the ability of each model to recapitulate data varies between replicates. In the example MCF7 replicate (Fig 6A), model 1 has ΔAICs of 0.9 compared to model 2 and 81.3 compared to model 3, indicating that models 1 and 2 performed similarly in this case, while model 3 was substantially worse. In the example BT474 replicate (Fig 6B), model 1 has ΔAICs of 86.6 compared to model 2 and 332.8 compared to model 3, indicating that model 1 outperforms both models 2 and 3. In the MDA-MB-231 example replicate, model 1 has ΔAICs of -0.02 compared to model 2, indicating that this is one of the replicates in which model 2 outperforms model 1 (although the performance is quite similar, indicated by the very small ΔAICs of -0.02), and 2.8 compared to model 3, indicating that model 1 outperforms model 3. A more detailed investigation of the structure of these model preferences is available in **Text C Figures E and F in S1 File**). Critical time projections and model validation results are constructed using model 1.

Model validation

A leave-one-out cross validation [59] is used to test the predictive capability of model 1. Across 143,093 total points evaluated, 80.6% fall within the 95% confidence interval. These results are summarized in Table 3, with a more detailed breakdown in **Text D Table D in S1 File**.

Model performance varies between cell lines and with recovery status. Model 1 performs best in the MCF7 cell line (88% of data in the 95% confidence interval), less well in the MDA-MB-231 cell line (80.7% of data in the 95% confidence interval), and worst in the BT474 cell line (75.1% of data in the 95% confidence interval). Wells which recover are better modeled (89.8% of data within the 95% confidence interval) than wells which do not (62.5% of data

Table 3. Leave-one-out cross validation. The performance of model 1 at predicting data excluded from the training set is broken down by cell line and whether the replicate culture recovered or not (see Fig 4).

Condition	Points Evaluated	Within 95% CI
Overall	143093	80.6%
All cell lines, recovering wells	94824	89.8%
All cell lines, dying wells	48269	62.5%
MCF7 cell line, total	42442	88.0%
MCF7 cell line, recovering wells	25992	94.5%
MCF7 cell line, dying wells	16450	77.7%
BT474 cell line, total	56923	75.1%
BT474 cell line, recovering wells	41391	87.3%
BT474 cell line, dying wells	15532	42.4%
MDA-MB-231 cell line, total	43728	80.7%
MDA-MB-231 cell line, recovering wells	27441	89.1%
MDA-MB-231 cell line, dying wells	16287	66.4%

https://doi.org/10.1371/journal.pcbi.1009104.t003

within the 95% confidence interval). These results indicate that model 1 captures a significant portion (but not all) of the variation in the population level response to doxorubicin.

Critical time projection

After doxorubicin treatment, the cancer cell populations varied in rate of cell number decrease, lag time to net re-growth, and re-growth rate (**Fig 3**). Some cell populations remain quiescent and never initiate re-growth within the time of the experiment (**Fig 4**). To allow consistent comparison across the range of conditions explored in these experiments, we define a cell population as having recovered from the drug perturbation at the time, referred to as the critical time, when the population reaches twice the initial cell number for that replicate culture. In some cultures, regrowth to twice the original cell number is not observed before the end of the experiment. To enable the inclusion of these results, we use model projections of the critical time based on the best-fit curve of the optimal model identified by model selection.

As the concentration of doxorubicin in a single exposure increases, the critical time increases in all three cell lines (**Fig 7A, 7D, and 7G**). When the interval between two 75 nM doxorubicin exposures is varied in the MCF7 cell line (**Fig 7B**), and when the interval between two 200 nM doxorubicin exposures is varied in the MDA-MB-231 cell line (**Fig 7H**), a peak in the critical time is observed for both cell lines at a two day inter-treatment interval; this suggests that the cell population is sensitized to retreatment at this time. This result is consistent with the observation that 9/12 replicate cultures treated with this regimen in the MCF7 cell line and 6/12 replicate cultures treated with this regimen in the MDA-MB-231 cell line never recover (**Fig 4B and 4H**), and with the observation that the period of growth arrest is elevated at this time (**Fig 5B and 5H**). The maximum elevation in critical time to an average of 112.6 days in the MCF7 line and 55.8 days in the MDA-MB-231 line represent increases of 239% and 40% when compared to critical times obtained after a second treatment after 16 days or 10 days, respectively. When the interval between two 35 nM doxorubicin exposures is varied in the BT474 cell line, the critical time is elevated at intervals of zero to eight days (**Fig 7E**), which is consistent with the elevated period of growth arrest observed in these replicates (**Fig 5E**). The maximum elevation in critical time to an average of 46.0 days in the BT474 cell line represents an increase of 46% when compared to the average critical time after a second treatment at 16 days. When the number of sequential treatments with 75 nM doxorubicin and a two day inter-treatment interval in the MCF7 cell line is varied, the critical time increases on a second

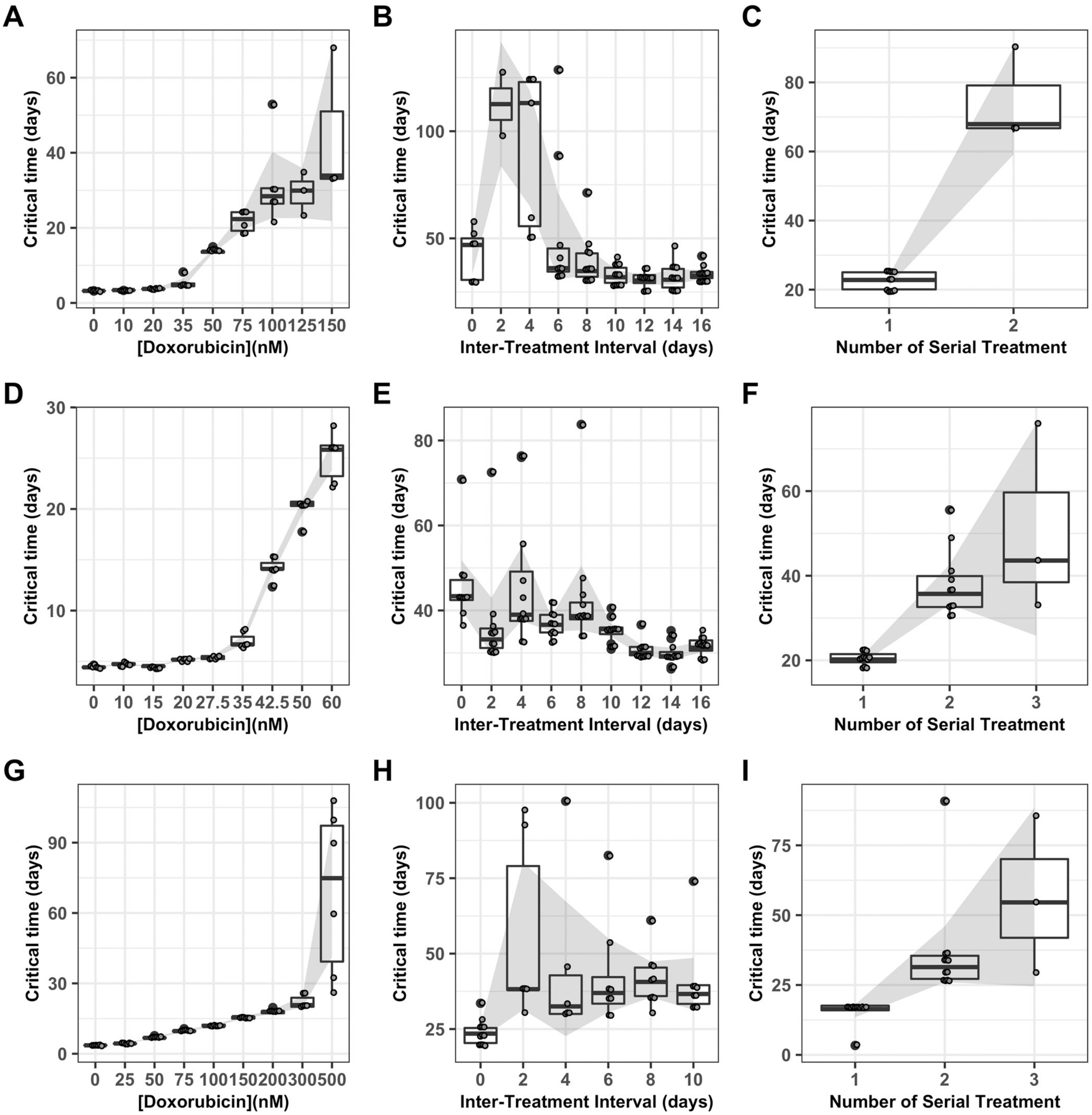

Fig 7. Critical time projections. Critical time is estimated based on the best fit to model 1 for each replicate culture in the MCF7 cell lines and shown as a Tukey box-and-whiskers plot as doxorubicin concentration varies in the MCF7 cell line (A), the BT474 cell line (D), and the MDA-MB-231 cell line (G), as the interval between two 24 hour doxorubicin exposures varies at 75 nM in the MCF7 cell line (B), at 35 nM in the BT474 cell line (E), and at 200 nM in the MDA-MB-231 cell line (H), and as the number of sequential 24 hour doxorubicin exposures varies at a two day interval and 75 nM in the MCF7 cell line (C), at a zero day interval (continuous exposure) and 35 nM in the BT474 cell line (F), and at a two day interval and 200 nM in the MDA-MB-231 cell line (I). The number of replicates in each group varies between 3 and 12; all replicates in which recovery is observed are included. The 95% confidence interval on the mean is shown by the shaded region.

https://doi.org/10.1371/journal.pcbi.1009104.g007

treatment (Fig 7C); the critical time for a third treatment cannot be obtained because no replicates treated with this regimen recovered (Fig 4C). When the number of sequential treatments with 35 nM doxorubicin and no inter-treatment interval is varied in the BT474 cell line, the critical time increases for the second and third treatment (Fig 7F), and cannot be obtained for the fourth and fifth treatment because too few replicate wells recovered. Similarly, when the number of sequential treatments with 200 nM doxorubicin and a two day inter-treatment interval is varied in the MDA-MB-231 cell line, the critical time increases after a second and third treatment, and cannot be obtained for the fourth treatment because no replicates treated with that regimen recovered (Fig 5I).

Discussion

The use of longitudinal monitoring *via* time-lapse microscopy allowed us to implement and compare dynamic models of drug sensitivity. This allowed us to identify conditions in which a model incorporating a delay on sensitive cell death is preferred over the more common, simpler model, and to determine that across the range of conditions tested, a model describing that delay with an exponential time constant performs best. Additionally, our model selection work identified the fraction of resistant cells (f_r) and the proliferation delay (t_r) as computationally non-separable. Quantification of t_r via automated clustering analysis confirmed the existence of a delay in proliferation under some conditions. Incorporating these two time delays removed sources of systematic error and allowed extraction of more accurate values for key model parameters such as the resistant fraction and post-recovery growth rate via calibration.

We identified transient changes in doxorubicin sensitivity following an initial doxorubicin exposure. Inter-treatment interval proved to be an optimizable factor in drug scheduling, with retreatment during the window of transient sensitivity increasing the total time to population doubling by 239% in the MCF7 line, 46% in the BT474 line, and 40% in the MDA-MB-231 line, compared to treatment with an identical total amount of drug with an interval such that drug sensitivity had stabilized. Because both drug concentration and number of sequential treatments tend to be more thoroughly explored in clinical application, inter-treatment interval represents an additional dimension on which drug dosing schedules can be optimized, and this may represent an opportunity to further improve the effectiveness of chemotherapeutic treatment in the clinic. In addition to extending the time to population doubling, treatment at the optimal time actually resulted in elimination of the cancer cell population in 9/12 replicate cultures in the MCF7 cell line, 1/12 replicate cultures in the BT474 cell line, and 6/12 replicate cultures in the MDA-MB-231 cell line. A number of hypotheses could explain the lesser relative improvement seen in the BT474 cell line, but it is likely that this results at least partly from the difference in the relative dose range used in this cell line; in both the MCF7 and MDA-MB-231 cell lines, the inter-treatment interval and serial dosing experiments were carried out at drug concentrations that resulted in a proliferation delay ($t_r > 0$), while in the BT474 line these experiments were carried out at a dose that did not consistently produce a proliferation delay. This suggests that the threshold for proliferation delay could play a key role in determining treatment effectiveness. It is also plausible that differences between the cell lines play a role in the differences we observed as well, and additional experimentation would be necessary to determine the relative importance of these factors. The optima identified for these cell lines did not depend on any single model parameter; they result from the interaction of all three relevant parameters, each of which changes dynamically with a different characteristic time.

In order to compare the performance of treatments varying in the rate of cell number decrease, lag time to net re-growth, and re-growth rate, we utilized the critical time metric, defined as the time at which a cell population reaches double its initial population. This definition prioritizes the long term regrowth of a culture over its immediate response; for example, a culture which experiences a small decline in total population, but very slow regrowth, could be identified as having a longer recovery time than a culture which experiences a steep drop in population but very rapid regrowth. Utilizing a definition of cancer cell recovery or progression based on regrowth relative to the initial population has been found to avoid counterintuitive results [60]. This definition also enables comparison of cultures which do not experience a drop in total population, but which do vary in growth rate, such as those exposed to a low concentration of doxorubicin (**Fig 3A**).

Although this mathematical modeling-based approach enabled the identification of key features of the dynamic response which have previously not been recognized (i.e., the time delays on both death and proliferation) it does have limitations. While model 1 was selected over the existing bi-exponential model in all three cell lines, the improvement in performance varied with cell line. The calibrated model allowed identification of optimal retreatment intervals in the MCF7 and MDA-MB-231 cell lines, but did not offer a clear equivalent in the BT474 cell line. This is likely due to differences in drug sensitivity and timing of response that characterize each cell line–BT474 has higher sensitivity and responds more slowly; consequently it was treated at a lower dose range. It is likely that the optimal model to describe growth dynamics varies with cell line, and possible that the most relevant mechanisms of changing drug sensitivity vary with cell line. A second significant limitation of this approach is that it is phenomenological, and while it does not require knowledge of the underlying mechanism, it also doesn't produce direct evidence to elucidate the mechanism(s).

While these results do not bear directly on the mechanisms of doxorubicin induced cell death, they are more compatible with some conclusions than others. Doxorubicin has multiple known mechanisms of action, and the relative contributions of each are not known under most circumstances [61]. The selection of model 1, with an exponential delay in the onset time of cell death, as the model best characterizing our data set suggests that mitotic catastrophe may play a larger role than other mechanisms such as doxorubicin-induced apoptosis which has a more defined time course and would have been more consistent with the linear time delay of model 2. It is likely that both processes are present, but mitotic catastrophe may be playing a larger role, particularly in the early part of the response where our modeling framework is most sensitive to t_d. Because no tests were performed to actually quantify the mechanisms of cell death in these experiments, this conclusion must be considered speculative. We anticipate that due to variations in the mechanism of action between different drugs, and even for a single drug between different dosing regimes, the resulting best model selected by our framework would also vary.

An additional limitation imposed by the experimental methods used here emerges from the need to calibrate models using only the total cell population, which limits the complexity of model which can be effectively calibrated. Models including additional subpopulations would improve the correspondence to the underlying biological system. Visual observation of the experimental cultures leads us to suspect that in addition to the sensitive cells which die and the resistant cells which recover proliferative capacity during the course of the experiment, there may be a subpopulation which persists in an arrested state throughout the course of the experiment. It is also plausible that some cell populations include more than two phenotypic subpopulations with different drug sensitivities, and depending on the drug schedule administered these subpopulations could vary in all relevant parameters—the resistant fraction, post-treatment growth rate, sensitive cell death rate, and the time constant for the death delay. Our framework, with a single sensitive population and a single resistant population, extracts parameters that represent a sort of population average in these parameters—e.g. if there are multiple resistant subpopulations which are growing at different rates, when we calibrate a single post-treatment growth rate to the total cell number curve, we extract a value that averages over the population and time course throughout the entire experiment. An experimental and computational framework that could resolve additional subpopulations would allow the exploration of these unresolved questions and improve our ability to identify the subpopulations most important to the development of chemoresistance. Such an improved framework is likely to require the development of novel experimental strategies to obtain time-resolved quantification of some relevant subpopulation marker or cellular property. This is necessary to ensure the uniqueness of solutions with additional subpopulations. Our framework is able to characterize one sensitive and one resistant population from a single output, the total cell number, due to the variation in sensitivity to each parameter over the time course of the experiment. To model additional subpopulations is likely to require an additional output variable.

In the experiments described here, substantial variability is observed in the population level responses (**Figs 3 and 4**), in the extracted parameters (**Fig 5**), and in the resulting metric for drug schedule performance (**Fig 7**). While experimental error can result in some variability, differences in the degree of variability within a single experiment (e.g. **Fig 3A**) suggest that much of the variation observed represents genuine divergences in the drug response between replicate populations. This results at least partially from stochasticity, both at the level of differences in subpopulation distribution in replicate populations and at the level of stochasticity in drug response, cell survival, and post-treatment proliferation. This stochasticity is captured as variability in extracted parameter values (**Fig 5**); rather than considering the variation of parameter values as reflecting measurement error, we view it as capturing the distribution of responses resulting from this stochasticity. This stochasticity could be further investigated by performing experiments with identical drug dosing schedules while varying the population size, since stochasticity results from the relative values of population frequency and population size. Variability should decline as the population size of each replicate is increased.

Despite the limitations discussed above, the framework outlined here could have applicability to future preclinical studies of chemotherapeutic dosing. Using an iterative experimental process to explore the relationship between drug concentration, inter-treatment interval, number of doses, and metrics such as the fraction of non-recovering replicates or critical time would allow the identification of optimal in vitro dosing schedules. In a purely in vitro setting this might mean searching for a minimum in the total integrated dose to accomplish the elimination of all cultures. When looking to shift into *in vivo* experimentation, however, the minimum total dose may not be the ideal metric because just as we have found that cancer cell drug sensitivity changes dynamically, chemotherapeutic toxicity to healthy tissue may also have a dynamic evolution over time. Therefore, it would be necessary to obtain information about *in vivo* toxicity and to use this to restrict the parameter space explored in *in vitro* experimentation and to guide the selection of the optimization's objective function. This would generate a dosing schedule tested *in vitro* which would be predicted to have optimal performance *in vivo*; this schedule wouldn't be expected to actually deliver optimal performance *in vivo*, due to the multitude of additional influences on *in vivo* drug behavior. It would, however, give an initial guess from which to start optimization of *in vivo* performance.

The approach described here allows for high throughput, high time resolution measurement of population-averaged properties. In particular, multidrug treatment would greatly benefit from longitudinal monitoring of population dynamics. Collateral sensitivity, a phenomenon where one drug causes a cell population to become sensitive to a second drug [62], has shown increasing promise *in-vitro* [63,64]. Notably, Dhawan et al. found that specific intervals between drugs was necessary in order to identify pairs of collaterally sensitive drugs. Furthermore, the repeatability of collateral sensitivity to drug-resistant populations has yet to be fully understood [65,66]. Thus, being able to perform high throughput measurement would allow for pairs of collaterally sensitive drugs to not only be found but evaluated as potential treatments. Additionally, the approach demonstrated here would allow for optimal control theory to be experimentally evaluated, a strategy which can be used to find optimal treatment strategies for a dynamical system [67]. Optimal control theory requires a detailed and accurate understanding of the relationship between controllable variables such as drug concentration and inter-treatment interval and biological variables such as the resistant fraction and post-treatment regrowth rate. The experimental and computational methods described here allow for the development of such detailed data sets. Optimal control theory has recently been used to find optimal scheduling [68,69], but has yet to be evaluated in an *in-vitro* setting. The development of drug response models with sufficient detail for use in predicting collateral sensitivity and testing optimal control theory could additionally contribute to the field of adaptive therapy, in which treatment is modified based on feedback regarding a patient's individual response [70]. This approach currently shows significant promise in the treatment of prostate cancer [71], and the development of more detailed drug response models can contribute to the extension of these techniques to additional cancer types. Single cell sequencing technologies promise to provide great insight into the mechanistic underpinnings of this heterogeneity in drug sensitivity [66,72]; however, throughput for these technologies remains low enough (and expense remains high enough) that directly assessing dynamic changes in drug sensitivity over short time scales remains difficult.

These two approaches can complement each other, with longitudinal studies such as the ones described here identifying key time scales and single cell transcriptomic studies enhancing mechanistic insight. This suggests several potentially productive avenues for continuing work: Additional longitudinal studies can extend the techniques demonstrated here to new drugs, new cell lines and new cancer types. Along with the development of new data sets, exploration of additional cancer growth models will allow deeper understanding of what features of a cell line (drug sensitivity, growth rate, clonal heterogeneity, etc.) correspond to particular optimal growth models. The data presented here also indicate time points that would be of particular interest for future single-cell studies, such as the two day post treatment optimal treatment interval in the MCF7 and MDA-MB-231 cell lines. Such studies could elucidate the mechanisms underlying these early changes in drug sensitivity, and could in turn enable another generation of longitudinal studies in cell lines engineered with fluorescent reporters coupled to mechanisms thus identified.

Finally, while these methods are several steps removed from clinically actionable at this point, there is potential to contribute to preclinical drug development. *In vitro* mechanistic studies and preclinical screening often report cell death at a single end point 24–72 hours after treatment; this is insufficient to quantify the long-term drug response of the cell population. Longitudinal studies such as these, implemented iteratively to identify key time scales such as the optimal inter-treatment interval, could allow further optimization of drug treatment schedules to inform preclinical testing.

Methods

Cell culture

MCF7 (ATCC HTB-22) cells were cultured in Minimum Essential Media (MEM) (Gibco), supplemented with 10% fetal bovine serum (FBS) and 1% penicillin-streptomycin (P/S) (Gibco); these cells were maintained at 37° C in a 5% CO_2 atmosphere [73]. BT474 (ATCC HTB-20) cells were cultured in Richter's Modification MEM (IMEM) (Corning), supplemented with 10% FBS, 1% P/S, and 20 μg/mL insulin; these cells were maintained at 37° C in a 5% CO_2 atmosphere [74]. MDA-MB-231 (ATCC HTB-26) cells were cultured in Dulbecco's Modified Eagle Media (DMEM) (Gibco) supplemented with 5% FBS and 1% P/S; these cells were maintained at 37° C in a 5% CO_2 atmosphere [75].

To facilitate the use of fluorescent microscopy and automated cell quantification, stable fluorescent cell lines were established (MCF7-EGFPNLS1, BT474-GNS2, 231-GNS) expressing constitutive EGFP with a nuclear localization signal. Genomic integration of the EGFP expression cassette was accomplished utilizing the Sleeping Beauty transposon system. The EGFP-NLS sequence was obtained as a gBlock (IDT) and cloned into the optimized Sleeping Beauty transfer vector pSBbi-Neo. pSBbi-Neo was a gift from Eric Kowarz (Addgene plasmid #60525) [76]. To mediate genomic integration, this two-plasmid system consisting of the transfer vector containing the EGFP-NLS sequence and the pCMV (CAT)T7-SB100 plasmid containing the Sleeping Beauty transposase was co-transfected into the MCF-7 population utilizing Lipofectamine 2000. mCMV (CAT)T7-SB100 was a gift from Zsuzsanna Izsvak (Addgene plasmid # 34879) [77]. Following gene integration with Sleeping Beauty transposase, eGFP+ cells were collected by fluorescence activated cell sorting and maintained in media supplemented with 200 ng/mL G418 in place of P/S.

Doxorubicin treatment

Doxorubicin hydrochloride (Cayman Chemical 15007) is reconstituted in water. Cell culture media is replaced with complete growth media containing doxorubicin at the specified concentration. After 24 hours, doxorubicin media is replaced with drug-free media.

Long term doxorubicin response experiments

Cells are seeded in a 96-well plate at target densities of 2,000 cells per well. Fluorescent and phase contrast images are collected at intervals of 4 hours or shorter throughout the study in the Incucyte S2 Live Cell Analysis System (Essen/Sartorius) with temperature and environmental control. Cells are initially seeded in 100 μL growth media per well and cultured for 2 days to allow cell adhesion and recovery from the passaging process. Drug treatment is performed by adding 100 μL growth media containing doxorubicin at 2x the desired final concentration, with 6 or 12 replicates for each experimental condition. After 24 hours, the drug exposure is ended by aspirating the media, and replacing with fresh growth media. Images collection is continued for 21–56 days at a frequency between once per two hours and once per four hours; the duration of image collection is selected such that all wells in which any cells recover proliferation are allowed to reach the logistic growth stage.

Model identifiability analysis

To test the ability of our modeling framework to accurately extract parameter values and select among models, each model within the family described above was used to calibrate simulated data. This model family includes three sets of assumptions concerning the form of k, which are described as models 1, 2, and 3; independently, t_r can be zero or non-zero. Six simulated data sets, labeled A through F and each containing 1000 time series of cell number, were generated from these six sets of assumptions concerning the underlying ground truth. For each data set, parameter values were randomly generated from within a physiologically reasonable parameter space (details provided in **Text A in S1 File),** a cell number vector was generated based on those parameter values, and Gaussian random noise was added to each data point of the cell number vector to simulate measurement error. We were interested in determining whether the underlying model could be identified from the cell number data alone, or whether the t_r

Table 4. Summary of model assumptions tested in model identifiability analysis.

Model	Assignment of t_r, proliferation delay in R cells	k, death delay in S cells	N_{max}
1	known and given as input	Exponential	Calibrated
2	known and given as input	Linear	Calibrated
3	known and given as input	None	Calibrated
4	calibrated	Exponential	Calibrated
5	calibrated	Linear	Calibrated
6	calibrated	None	Calibrated
7	0	Exponential	Calibrated
8	0	Linear	Calibrated
9	0	None	Calibrated
10	known and given as input	Exponential	Fixed
11	known and given as input	Linear	Fixed
12	known and given as input	None	Fixed
13	calibrated	Exponential	Fixed
14	calibrated	Linear	Fixed
15	calibrated	None	Fixed
16	0	Exponential	Fixed
17	0	Linear	Fixed
18	0	None	Fixed

https://doi.org/10.1371/journal.pcbi.1009104.t004

value must also be specified to obtain accurate parameter values. Additionally, we sought to determine whether it was possible to reduce the number of free parameters by fixing N_{max}. This resulted in a total of 18 models: k selected from models 1, 2, or 3, t_r calibrated, assumed to be 0, or given as input, and N_{max} either calibrated or fixed. Each data set was used to calibrate the 18 models, summarized in Table 4.

To check the ability of each model to extract accurate parameter values from the simulated data sets, Pearson's correlation coefficients (PCC) between the known and calibrated values for the model parameters were computed for each combination of model and simulated data set (**Text C Table C in** S1 File).

The Akaike information criterion was applied to the calibrations generated by models 1–3 on simulated data sets A-F to test its ability to identify the underlying model structure in cases where the ground truth is known independently.

Image analysis

Cell counting is performed using the green fluorescence channel using standard image analysis techniques: background subtraction, followed by thresholding, edge detection, and a minimum area filter. These settings have been optimized for accuracy and robustness in handling the image-to-image variation in acquired images. Due to variations in cell brightness and nucleus size which occur after doxorubicin exposure, the optimal image processing parameters vary from experiment to experiment. The processing definition is therefore optimized iteratively for each experiment, with visual checks of a sample of the processed images used to confirm the accuracy of cell counting. A detailed description of the recommended optimization process is provided as **Text E in** S1 File.

Data normalization

The data for each replicate culture is truncated to ensure that only accurate, meaningful data is used for model calibration. Time course cell number data for each replicate culture is truncated at 30,000 cells or when the counted cell number drops by more than 50% as a result of media handling, or when the cell count becomes unreliable as indicated by repeated discontinuities in the cell number vector. In the case of a single discontinuity where fewer than half of the cells are lost, the data is instead normalized to remove the discontinuity; this normalization is performed by specifying that the cell number for time points prior to the discontinuity will be divided by a constant α, calculated such that the first and second derivative of the cell number are smooth across the discontinuity:

$$\alpha = \frac{\frac{(N_{d-1}-N_{d-2})}{(t_{d-1}-t_{d-2})} + 2\frac{N_{d-1}}{t_d-t_{d-1}}}{2\frac{N_d}{t_d-t_{d-1}} + \frac{N_d-N_{d+1}}{t_{d+1}-t_d}}$$

Here N_d is the cell number just after the discontinuity, N_{d-1} is the cell number just before the discontinuity, and so on.

Quantification of t_r

To find the proliferation delay, t_r, a density-based clustering technique (DBSCAN) was used to find an initial clustering of cells after treatment had been applied. The optimal parameters for DBSCAN were manually calibrated for each plate. Once a sufficiently large cluster of cells was properly identified, the cluster was tracked backwards in time. At each previous timepoint, DBSCAN was again used to identify the location of the cluster. When a timepoint was identified at which clustering could no longer be found, the proliferation delay was determined as the difference in hours between that timepoint and the time of initial treatment.

Model calibration

Model parameters are extracted from time course cell population data by calibrating the three models to the cell number vector for each replicate culture using a nonlinear least-squares approach (“lsqnonlin”) implemented in MATLAB.

Calculation of AIC

The residual sum of squares (RSS) after model calibration, the number of data points in the replicate n, and the model parameter number p, are used to calculate the AIC using Eq 9. The AIC also includes an arbitrary constant, C_{arb}, which we omit in calculations because model selection is performed based on ΔAIC.

$$AIC = 2p + n * ln(RSS) + C_{arb} \tag{9}$$

Critical time projection

In replicates where the cell population reaches double the replicate’s original population during the course of the experiment, the critical time is identified as the first time at which the number of cells is greater than or equal to double the starting population. However, in some cultures regrowth to twice the original cell number is not observed before the end of the experiment. To enable the inclusion of these results, we use model projections of the critical time based on the best-fit curve of the optimal model identified by model selection. Critical time projections are carried forward for a maximum of one year; replicates in which the population is not projected to reach double its initial value within one year are marked as not recovering.

Supporting information

S1 File. Text A. Model identifiability results. **Table A**. Model assumptions used to generate simulated data sets. **Table B**. Parameter distributions for simulated data sets. **Figure A**. Model performance on data with no proliferation delay. **Figure B**. Model performance on data with a proliferation delay. **Figure C**. Model performance with fixed vs. calibrated carrying capacity. **Figure D**. Model performance on matched and mismatched death delay assumptions. **Table C**. Model performance summarized via PCC. **Text B**. Constraining the model calibration. **Text C**. Structure of model preferences. **Figure E**. Selection of model 1 over model 2. **Figure F**. Selection of model 1 over model 3. **Text D**. Details of Model Validation Results. **Table D**. Leave-one-out validation of model 1 calibration results. **Text E**. Processing Definition Optimization in the Incucyte Zoom.
(PDF)

Acknowledgments

We would like to thank Yasmeen K. Zubair and Isha Patel for their work in data collection and processing during the preliminary experiments which initiated this work. A.B. is grateful to Jeff Brock for sharing remote work space throughout the preparation of this manuscript.

Author Contributions

Conceptualization: Grant R. Howard, Amy Brock.

Data curation: Grant R. Howard, Tyler A. Jost.

Formal analysis: Grant R. Howard, Tyler A. Jost.

Funding acquisition: Amy Brock.

Investigation: Grant R. Howard, Thomas E. Yankeelov.

Supervision: Thomas E. Yankeelov, Amy Brock.

Visualization: Grant R. Howard, Tyler A. Jost.

Writing – original draft: Grant R. Howard, Amy Brock.

Writing – review & editing: Grant R. Howard, Tyler A. Jost, Thomas E. Yankeelov, Amy Brock.

References

1. Heron M. Deaths: Leading Causes for 2017. Natl Vital Stat Rep. 2019 Jun 24; 68(6). PMID: 32501203
2. Longley DB, Johnston PG. Molecular mechanisms of drug resistance. J Pathol. 2005 Jan; 205(2):275–92. https://doi.org/10.1002/path.1706 PMID: 15641020
3. McKenna MT, Weis JA, Brock A, Quaranta V, Yankeelov TE. Precision Medicine with Imprecise Therapy: Computational Modeling for Chemotherapy in Breast Cancer. Transl Oncol. 2018 Jun; 11(3):732–42. https://doi.org/10.1016/j.tranon.2018.03.009 PMID: 29674173
4. Jarrett AM, Lima EABF, Hormuth DA, McKenna MT, Feng X, Ekrut DA, et al. Mathematical Models of Tumor Cell Proliferation: A Review of the Literature. Expert Rev Anticancer Ther. 2018 Dec; 18(12):1271–86. https://doi.org/10.1080/14737140.2018.1527689 PMID: 30252552
5. Altrock PM, Liu LL, Michor F. The mathematics of cancer: integrating quantitative models. Nat Rev Cancer. 2015 Dec; 15(12):730–45. https://doi.org/10.1038/nrc4029 PMID: 26597528
6. Moreno L, Pearson AD. How can attrition rates be reduced in cancer drug discovery? Expert Opin Drug Discov. 2013 Apr 1; 8(4):363–8. https://doi.org/10.1517/17460441.2013.768984 PMID: 23373702
7. Le Tourneau C, Lee JJ, Siu LL. Dose Escalation Methods in Phase I Cancer Clinical Trials. JNCI J Natl Cancer Inst. 2009 May 20; 101(10):708–20. https://doi.org/10.1093/jnci/djp079 PMID: 19436029

8. Gottlieb JA, Rivkin SE, Spigel SC, Hoogstraten B, O'Bryan RM, Delaney FC, et al. Superiority of adriamycin over oral nitrosoureas in patients with advanced breast carcinoma. A southwest cancer chemotherapy study group study. Cancer. 1974; 33(2):519–26. https://doi.org/10.1002/1097-0142(197402)33:2<519::aid-cncr2820330229>3.0.co;2-x PMID: 4812769

9. Brock A, Chang H, Huang S. Non-genetic heterogeneity—a mutation-independent driving force for the somatic evolution of tumours. Nat Rev Genet. 2009 May; 10(5):336–42. https://doi.org/10.1038/nrg2556 PMID: 19337290

10. Turashvili G, Brogi E. Tumor Heterogeneity in Breast Cancer. Front Med. 2017; 4:227. https://doi.org/10.3389/fmed.2017.00227 PMID: 29276709

11. Abramson VG, Mayer IA. Molecular Heterogeneity of Triple Negative Breast Cancer. Curr Breast Cancer Rep. 2014 Sep 1; 6(3):154–8. https://doi.org/10.1007/s12609-014-0152-1 PMID: 25419441

12. Bedard PL, Hansen AR, Ratain MJ, Siu LL. Tumour heterogeneity in the clinic. Nature. 2013 Sep; 501(7467):355–64. https://doi.org/10.1038/nature12627 PMID: 24048068

13. Burrell R, Mcgranahan N, Bartek J, Swanton C. The Causes and Consequences of Genetic Heterogeneity in Cancer Evolution. Nature. 2013 Sep 19; 501:338–45. https://doi.org/10.1038/nature12625 PMID: 24048066

14. Wolman SR, Heppner GH. Genetic heterogeneity in breast cancer. J Natl Cancer Inst. 1992 Apr 1; 84(7):469–70. https://doi.org/10.1093/jnci/84.7.469 PMID: 1545431

15. Brooks MD, Burness ML, Wicha MS. Therapeutic Implications of Cellular Heterogeneity and Plasticity in Breast Cancer. Cell Stem Cell. 2015 Sep 3; 17(3):260–71. https://doi.org/10.1016/j.stem.2015.08.014 PMID: 26340526

16. Håkansson L, Tropé C. On the Presence Within Tumours of Clones That Differ in Sensitivity to Cytostatic Drugs. Acta Pathol Microbiol Scand [A]. 1974; 82A(1):35–40. https://doi.org/10.1111/j.1699-0463.1974.tb03825.x PMID: 4827349

17. Davila E, Amazon K. The Clinical Importance of the Heterogeneity of HER2 neu. Case Rep Oncol. 2010; 3(2):268–71. https://doi.org/10.1159/000319020 PMID: 21045934

18. McGranahan N, Swanton C. Biological and Therapeutic Impact of Intratumor Heterogeneity in Cancer Evolution. Cancer Cell. 2015 Jan 12; 27(1):15–26. https://doi.org/10.1016/j.ccell.2014.12.001 PMID: 25584892

19. Norton L, Simon R. Tumor size, sensitivity to therapy, and design of treatment schedules. Cancer Treat Rep. 1977 Oct; 61(7):1307–17. PMID: 589597

20. Norton L, Simon R. Growth curve of an experimental solid tumor following radiotherapy. J Natl Cancer Inst. 1977 Jun; 58(6):1735–41. https://doi.org/10.1093/jnci/58.6.1735 PMID: 194044

21. Norton L, Simon R. The Norton-Simon hypothesis revisited. Cancer Treat Rep. 1986 Jan; 70(1):163–9. PMID: 3510732

22. Bonadonna G, Zambetti M, Valagussa P. Sequential or alternating doxorubicin and CMF regimens in breast cancer with more than three positive nodes. Ten-year results. JAMA. 1995 Feb 15; 273(7):542–7. PMID: 7837388

23. Bonadonna G, Zambetti M, Moliterni A, Gianni L, Valagussa P. Clinical relevance of different sequencing of doxorubicin and cyclophosphamide, methotrexate, and Fluorouracil in operable breast cancer. J Clin Oncol Off J Am Soc Clin Oncol. 2004 May 1; 22(9):1614–20.

24. Citron ML, Berry DA, Cirrincione C, Hudis C, Winer EP, Gradishar WJ, et al. Randomized trial of dose-dense versus conventionally scheduled and sequential versus concurrent combination chemotherapy as postoperative adjuvant treatment of node-positive primary breast cancer: first report of Intergroup Trial C9741/Cancer and Leukemia Group B Trial 9741. J Clin Oncol Off J Am Soc Clin Oncol. 2003 Apr 15; 21(8):1431–9.

25. Liu Y, Gu F, Liang J, Dai X, Wan C, Hong X, et al. The efficacy and toxicity profile of metronomic chemotherapy for metastatic breast cancer: A meta-analysis. PloS One. 2017; 12(3):e0173693. https://doi.org/10.1371/journal.pone.0173693 PMID: 28296916

26. Munzone E, Colleoni M. Clinical overview of metronomic chemotherapy in breast cancer. Nat Rev Clin Oncol. 2015 Nov; 12(11):631–44. https://doi.org/10.1038/nrclinonc.2015.131 PMID: 26241939

27. Hanahan D, Bergers G, Bergsland E. Less is more, regularly: metronomic dosing of cytotoxic drugs can target tumor angiogenesis in mice. J Clin Invest. 2000 Apr; 105(8):1045–7. https://doi.org/10.1172/JCI9872 PMID: 10772648

28. Kaur H, Budd GT. Metronomic therapy for breast cancer. Curr Oncol Rep. 2004 Jan; 6(1):49–52. https://doi.org/10.1007/s11912-996-0009-5 PMID: 14664761

29. Munoz R, Shaked Y, Bertolini F, Emmenegger U, Man S, Kerbel RS. Anti-angiogenic treatment of breast cancer using metronomic low-dose chemotherapy. Breast Edinb Scotl. 2005 Dec; 14(6):466–79. https://doi.org/10.1016/j.breast.2005.08.026 PMID: 16199161

30. Almeida L, Bagnerini P, Fabrini G, Hughes BD, Lorenzi T. Evolution of cancer cell populations under cytotoxic therapy and treatment optimisation: insight from a phenotype-structured model. ESAIM Math Model Numer Anal. 2019 Jul; 53(4):1157–90.

31. Greene JM, Sanchez-Tapia C, Sontag ED. Mathematical Details on a Cancer Resistance Model. Front Bioeng Biotechnol. 2020 Jun 17; 8. https://doi.org/10.3389/fbioe.2020.00501 PMID: 32656186

32. Olivier A, Pouchol C. Combination of Direct Methods and Homotopy in Numerical Optimal Control: Application to the Optimization of Chemotherapy in Cancer. J Optim Theory Appl. 2019 May 1; 181 (2):479–503.

33. Pouchol C, Clairambault J, Lorz A, Trélat E. Asymptotic analysis and optimal control of an integro-differential system modelling healthy and cancer cells exposed to chemotherapy. J Mathématiques Pures Appliquées. 2018 Aug 1; 116:268–308.

34. Howard GR, Johnson KE, Rodriguez Ayala A, Yankeelov TE, Brock A. A multi-state model of chemoresistance to characterize phenotypic dynamics in breast cancer. Sci Rep. 2018 Dec; 8(1):12058. https://doi.org/10.1038/s41598-018-30467-w PMID: 30104569

35. AbuHammad S, Zihlif M. Gene expression alterations in doxorubicin resistant MCF7 breast cancer cell line. Genomics. 2013 Apr; 101(4):213–20. https://doi.org/10.1016/j.ygeno.2012.11.009 PMID: 23201559

36. Gottesman MM. Mechanisms of cancer drug resistance. Annu Rev Med. 2002; 53:615–27. https://doi.org/10.1146/annurev.med.53.082901.103929 PMID: 11818492

37. Hill RP, Chambers AF, Ling V, Harris JF. Dynamic heterogeneity: rapid generation of metastatic variants in mouse B16 melanoma cells. Science. 1984 Jun 1; 224(4652):998–1001. https://doi.org/10.1126/science.6719130 PMID: 6719130

38. Kuukasjärvi T, Karhu R, Tanner M, Kähkönen M, Schäffer A, Nupponen N, et al. Genetic heterogeneity and clonal evolution underlying development of asynchronous metastasis in human breast cancer. Cancer Res. 1997 Apr 15; 57(8):1597–604. PMID: 9108466

39. Simpson PT, Reis-Filho JS, Gale T, Lakhani SR. Molecular evolution of breast cancer. J Pathol. 2005 Jan; 205(2):248–54. https://doi.org/10.1002/path.1691 PMID: 15641021

40. Balko JM, Giltnane JM, Wang K, Schwarz LJ, Young CD, Cook RS, et al. Molecular profiling of the residual disease of triple-negative breast cancers after neoadjuvant chemotherapy identifies actionable therapeutic targets. Cancer Discov. 2014 Feb; 4(2):232–45. https://doi.org/10.1158/2159-8290.CD-13-0286 PMID: 24356096

41. Duncan JS, Whittle MC, Nakamura K, Abell AN, Midland AA, Zawistowski JS, et al. Dynamic reprogramming of the kinome in response to targeted MEK inhibition in triple-negative breast cancer. Cell. 2012 Apr 13; 149(2):307–21. https://doi.org/10.1016/j.cell.2012.02.053 PMID: 22500798

42. Navin N, Krasnitz A, Rodgers L, Cook K, Meth J, Kendall J, et al. Inferring tumor progression from genomic heterogeneity. Genome Res. 2010 Jan; 20(1):68–80. https://doi.org/10.1101/gr.099622.109 PMID: 19903760

43. Levsky JM, Shenoy SM, Pezo RC, Singer RH. Single-cell gene expression profiling. Science. 2002 Aug 2; 297(5582):836–40. https://doi.org/10.1126/science.1072241 PMID: 12161654

44. Dalerba P, Kalisky T, Sahoo D, Rajendran PS, Rothenberg ME, Leyrat AA, et al. Single-cell dissection of transcriptional heterogeneity in human colon tumors. Nat Biotechnol. 2011 Dec; 29(12):1120–7. https://doi.org/10.1038/nbt.2038 PMID: 22081019

45. Jolly MK, Kulkarni P, Weninger K, Orban J, Levine H. Phenotypic Plasticity, Bet-Hedging, and Androgen Independence in Prostate Cancer: Role of Non-Genetic Heterogeneity. Front Oncol. 2018; 8:50. https://doi.org/10.3389/fonc.2018.00050 PMID: 29560343

46. Singh DK, Ku C-J, Wichaidit C, Steininger RJ, Wu LF, Altschuler SJ. Patterns of basal signaling heterogeneity can distinguish cellular populations with different drug sensitivities. Mol Syst Biol. 2010 May 11; 6:369. https://doi.org/10.1038/msb.2010.22 PMID: 20461076

47. Sigal A, Milo R, Cohen A, Geva-Zatorsky N, Klein Y, Liron Y, et al. Variability and memory of protein levels in human cells. Nature. 2006 Nov; 444(7119):643–6. https://doi.org/10.1038/nature05316 PMID: 17122776

48. Pisco AO, Brock A, Zhou J, Moor A, Mojtahedi M, Jackson D, et al. Non-Darwinian dynamics in therapy-induced cancer drug resistance. Nat Commun. 2013 Dec; 4(1):2467. https://doi.org/10.1038/ncomms3467 PMID: 24045430

49. Pisco AO, Huang S. Non-genetic cancer cell plasticity and therapy-induced stemness in tumour relapse: "What does not kill me strengthens me." Br J Cancer. 2015 May 26; 112(11):1725–32. https://doi.org/10.1038/bjc.2015.146 PMID: 25965164

50. Sharma SV, Lee DY, Li B, Quinlan MP, Takahashi F, Maheswaran S, et al. A chromatin-mediated reversible drug-tolerant state in cancer cell subpopulations. Cell. 2010 Apr 2; 141(1):69–80. https://doi.org/10.1016/j.cell.2010.02.027 PMID: 20371346

51. Flusberg DA, Roux J, Spencer SL, Sorger PK. Cells surviving fractional killing by TRAIL exhibit transient but sustainable resistance and inflammatory phenotypes. Mol Biol Cell. 2013 Jul; 24(14):2186–200. https://doi.org/10.1091/mbc.E12-10-0737 PMID: 23699397

52. Chatterjee MS, Elassaiss-Schaap J, Lindauer A, Turner DC, Sostelly A, Freshwater T, et al. Population Pharmacokinetic/Pharmacodynamic Modeling of Tumor Size Dynamics in Pembrolizumab-Treated Advanced Melanoma. CPT Pharmacomet Syst Pharmacol. 2017 Jan; 6(1):29–39. https://doi.org/10.1002/psp4.12140 PMID: 27896938

53. Hokanson JA, Brown BW, Thompson JR, Drewinko B, Alexanian R. Tumor growth patterns in multiple myeloma. Cancer. 1977 Mar; 39(3):1077–84. https://doi.org/10.1002/1097-0142(197703)39:3<1077::aid-cncr2820390311>3.0.co;2-s PMID: 912647

54. W K., et al. Precision medicine by modeling pharmacokinetic and biomarker drivers of tumor kinetics: assessing effects of alsertib exposure and target SNP status on antitumor activity. CPT Pharmacomet Syst Pharmacol. 2017; 101(S1):S5–99.

55. McKenna MT, Weis JA, Barnes SL, Tyson DR, Miga MI, Quaranta V, et al. A Predictive Mathematical Modeling Approach for the Study of Doxorubicin Treatment in Triple Negative Breast Cancer. Sci Rep. 2017 Jul 18; 7(1):5725. https://doi.org/10.1038/s41598-017-05902-z PMID: 28720897

56. Akaike H. A new look at the statistical model identification. IEEE Trans Autom Control. 1974 Dec; 19 (6):716–23.

57. Symonds MRE, Moussalli A. A brief guide to model selection, multimodel inference and model averaging in behavioural ecology using Akaike's information criterion. Behav Ecol Sociobiol. 2011 Jan; 65 (1):13–21.

58. Ester M, Kriegel H-P, Sander J, Xu X. A density-based algorithm for discovering clusters in large spatial databases with noise. In: Proceedings of the Second International Conference on Knowledge Discovery and Data Mining. Portland, Oregon; 1996. p. 226–31. (KDD'96).

59. Kuhn M, Johnson K. Applied Predictive Modeling. Springer New York; 2018. 600 p.

60. Johnson K, Gomez A, Burton J, White D, Chakravarty A, Schmid A, et al. Directional inconsistency between Response Evaluation Criteria in Solid Tumors (RECIST) time to progression and response speed and depth. Eur J Cancer. 2019 Mar 1; 109:196–203. https://doi.org/10.1016/j.ejca.2018.11.008 PMID: 30738696

61. Eom Y-W, Kim MA, Park SS, Goo MJ, Kwon HJ, Sohn S, et al. Two distinct modes of cell death induced by doxorubicin: apoptosis and cell death through mitotic catastrophe accompanied by senescence-like phenotype. Oncogene. 2005 Jul; 24(30):4765–77. https://doi.org/10.1038/sj.onc.1208627 PMID: 15870702

62. Pluchino KM, Hall MD, Goldsborough AS, Callaghan R, Gottesman MM. Collateral sensitivity as a strategy against cancer multidrug resistance. Drug Resist Updat. 2012 Feb; 15(1–2):98–105. https://doi.org/10.1016/j.drup.2012.03.002 PMID: 22483810

63. Dhawan A, Nichol D, Kinose F, Abazeed ME, Marusyk A, Haura EB, et al. Collateral sensitivity networks reveal evolutionary instability and novel treatment strategies in ALK mutated non-small cell lung cancer. Sci Rep. 2017 Dec; 7(1):1232. https://doi.org/10.1038/s41598-017-00791-8 PMID: 28450729

64. Acar A, Nichol D, Fernandez-Mateos J, Cresswell GD, Barozzi I, Hong SP, et al. Exploiting evolutionary steering to induce collateral drug sensitivity in cancer. Nat Commun. 2020 Apr 21; 11(1):1–14. https://doi.org/10.1038/s41467-019-13993-7 PMID: 31911652

65. Nichol D, Rutter J, Bryant C, Hujer AM, Lek S, Adams MD, et al. Antibiotic collateral sensitivity is contingent on the repeatability of evolution. Nat Commun. 2019 Dec; 10(1):334. https://doi.org/10.1038/s41467-018-08098-6 PMID: 30659188

66. Scarborough JA, McClure E, Anderson P, Dhawan A, Durmaz A, Lessnick SL, et al. Identifying States of Collateral Sensitivity during the Evolution of Therapeutic Resistance in Ewing's Sarcoma. iScience. 2020 Jul 24; 23(7):101293. https://doi.org/10.1016/j.isci.2020.101293 PMID: 32623338

67. Jarrett AM, Faghihi D, Ii DAH, Lima EABF, Virostko J, Biros G, et al. Optimal Control Theory for Personalized Therapeutic Regimens in Oncology: Background, History, Challenges, and Opportunities. J Clin Med. 2020 May 2; 9(5):1314.

68. Yoon N, Vander Velde R, Marusyk A, Scott JG. Optimal Therapy Scheduling Based on a Pair of Collaterally Sensitive Drugs. Bull Math Biol. 2018 Jul 1; 80(7):1776–809. https://doi.org/10.1007/s11538-018-0434-2 PMID: 29736596

69. Gluzman M, Scott JG, Vladimirsky A. Optimizing adaptive cancer therapy: dynamic programming and evolutionary game theory. Proc R Soc B Biol Sci. 2020 Apr 29; 287(1925):20192454. https://doi.org/10.1098/rspb.2019.2454 PMID: 32315588

70. Gatenby RA, Silva AS, Gillies RJ, Frieden BR. Adaptive Therapy. Cancer Res. 2009 Jun 1; 69 (11):4894–903. https://doi.org/10.1158/0008-5472.CAN-08-3658 PMID: 19487300

71. Brady-Nicholls R, Nagy JD, Gerke TA, Zhang T, Wang AZ, Zhang J, et al. Prostate-specific antigen dynamics predict individual responses to intermittent androgen deprivation. Nat Commun. 2020 Apr 9; 11(1):1750. https://doi.org/10.1038/s41467-020-15424-4 PMID: 32273504

72. Kim C, Gao R, Sei E, Brandt R, Hartman J, Hatschek T, et al. Chemoresistance Evolution in Triple-Negative Breast Cancer Delineated by Single-Cell Sequencing. Cell. 2018 May; 173(4):879–893.e13. https://doi.org/10.1016/j.cell.2018.03.041 PMID: 29681456

73. Soule HD, Vazguez J, Long A, Albert S, Brennan M. A human cell line from a pleural effusion derived from a breast carcinoma. J Natl Cancer Inst. 1973 Nov; 51(5):1409–16. https://doi.org/10.1093/jnci/51.5.1409 PMID: 4357757

74. Lasfargues EY, Coutinho WG, Redfield ES. Isolation of two human tumor epithelial cell lines from solid breast carcinomas. J Natl Cancer Inst. 1978 Oct; 61(4):967–78. PMID: 212572

75. Cailleau R, Olivé M, Cruciger QV. Long-term human breast carcinoma cell lines of metastatic origin: preliminary characterization. In Vitro. 1978 Nov; 14(11):911–5. https://doi.org/10.1007/BF02616120 PMID: 730202

76. Kowarz E, Löscher D, Marschalek R. Optimized Sleeping Beauty transposons rapidly generate stable transgenic cell lines. Biotechnol J. 2015 Apr; 10(4):647–53. https://doi.org/10.1002/biot.201400821 PMID: 25650551

77. Mátés L, Chuah MKL, Belay E, Jerchow B, Manoj N, Acosta-Sanchez A, et al. Molecular evolution of a novel hyperactive Sleeping Beauty transposase enables robust stable gene transfer in vertebrates. Nat Genet. 2009 Jun; 41(6):753–61. https://doi.org/10.1038/ng.343 PMID: 19412179